# High-Order Spectral Difference Simulation of Laminar Compressible Flow Over Two Counter-Rotating Cylinders

Kui Ou, [*] Chunlei Liang, [†] Sachin Premasuthan, [‡] and Antony Jameson [§]

*Aeronautics and Astronautics Department, Stanford University, CA 94305, USA*

**Flow past a single rotating cylinder has been studied, both numerically and experimentally, by many authors. In contrast is the flow past rotating cylinders in a side-by-side arrangement, which has only very limited numerical and experimental data available, despite the pioneering theoretical study by Jeffery[1] as early as 1922. In this paper, we discuss a numerical investigation of the steady laminar viscous flow past two infinite rotating cylinders in a side-by-side configuration. The solution of the compressible two-dimensional Navier-Stokes equations is determined numerically using the high-order spectral difference scheme over an unstructured qudralateral grid. Third order accurate results in both time and space were obtained and compared with existing data. In addition to obtaining a high-order accurate result for flow past two rotating cylinders, we extend the current numerical effort to investigate the effects of Reynolds number, compressibility, and high rotation speed, which have not been comprehensively studied in the past.**

## I.   Introduction

The problem of viscous fluid flow around two circular cylinders rotating side-by-side to each other is not a new one, but certainly an interesting one that has attracted many researchers. Jeffery[1] first discussed an analytical treatment of the rotation of two circular cylinders in a viscous flow in 1922 using the Stoke approximation. He showed that, in the special case of two disjoint equal cylinders of radius r, at a center-to-center distance d apart, counter-rotating at the same speed $\omega$ in an infinite viscous fluid, the far-field flow will assume an steady uniform motion $U_\infty = \frac{\omega r^2}{d}$, and the net force acting on the cylinders will be zero. However, Jeffery's solution in bi-polar co-ordinates of the two-dimensional Stokes equations omitted other Stokes solutions which could give rise to non-zero net force on the cylinders. Watson[2] made up for this deficiency by including additional fourier serial terms in his refined treatment of such flow, and found that, in higher order approximation, the special case of equal counter-rotating cylinders, like before, has a steady far field motion, but this time with non-vanishing force acting normal to the line of centers of the cylinders. The nature of the investigation, however, has remained mainly theoretical and mathematical.[3,4] With current Computational Fluid Dynamic capability, the characteristics of this special flow can certainly be more fully quantified numerically by solving the full governing equations with a high-order accurate scheme, hence the motivation of the present study.

Despite considerable studies on flow past a single rotating cylinder, comparable work to numerically and experimentally understand the physics of flow over two rotating cylinders have been very few. Elliott[6] had used a boundary element method to compute the streamline and vorticity patterns for such kind of flow, but his method also produced results with zero net force on the cylinders. Nakanishi and Kida[5] implemented a vortex method to study impulsively started counter-rotating cylinders pair of equal radii in fluid initially at rest, in an effort to understand the mechanism of the generation of the uniform flow due to cylinders rotation. Hills[7] carried out both experimental and numerical studies of two disjoint rotating cylinders in

---

[*]Doctoral Candidate, Department of Aeronautics and Astronautics, Stanford University, AIAA Member.
[†]PostDoc, Department of Aeronautics and Astronautics, Stanford University, AIAA Member.
[‡]Doctoral Candidate, Department of Aeronautics and Astronautics, Stanford University, AIAA Member.
[§]Thomas V. Jones Professor, Department of Aeronautics and Astronautics, Stanford University, AIAA Fellow.

two-dimensional newtonian fluid, but in a confined rectangular box without freestream flow. More elaborated computational studies to understand the flow characteristics of stream over two rotating cylinders were carried out by Surattana and Nikolay,[8] and Yoon, Kim, and Chun.[9] In the former, an incompressible two-dimensional Navier-Stokes equation in the cylindrical bipolar coordinate system was solved using projection methods based algorithm by Chorin.[10] Simulations were performed at low angular rotation speeds and Reynolds number to determine the resultant force on the cylinders. In the later, the combined effects of the rotation speed and the spacing between two cylinders were studied with the incompressible immersed boundary method, but again only low rotation speeds were considered at a fixed Reynolds number. Flow for rotation at high speeds was only recently studied by Chan and Jameson[11] with an industrial code, and they observed a virtual elliptic pattern that strongly resembles a doublet potential flow at fast enough rotation speeds.

The objective of the present work is to apply the recently developed high-order spectral difference method to complement and improve upon the numerical efforts that have been done before. We note that the numerical methods used for the above applications were limited to low order schemes and incompressible solvers. With a lack of experiment data on flow over the side-by-side counter-rotating cylinder pair, and in an effort to more accurately represent the physics of such kind of fluid motion, it proves advantageous to apply a higher order accurate scheme to this problem. In our present work, the compressible two-dimensional Navier-Stokes equation was solved with the spectral difference scheme over an unstructured qudralateral grid. Spline curve fitting was implemented along the cylindrical wall to achieve a high boundary resolution.

In particular, the current paper discusses the following aspects of two rotating cylinders flow: (1) the effect of rotation speed; (2) the effect of Reynolds Number; (3) the effect of compressibility; (4) the critical operating points for drag reduction, self-propulsion, and wake suppression; (5) the pressure contours and streamline patterns.

This paper is organized into 5 sections. We started by a brief introduction of the spectral difference method in the *Spectral Difference Method* section, followed by the actual numerical implementation of the method in *Numerical Formulation*. In the *Accuracy Validation* section, we computed flow past non-rotating cylindrical bodies, and compared our spectral difference results with the existing literatures. The main findings are discussed in the *Results and Discussions* section. In this section, we started by comparing and validating current numerical results on flow past two rotating cylinders, then went on to investigate the flow as outlined in the previous paragraph. In the *Conclusion* section, we summarize our high-order method results, and identify the main features of flow past two side-by-side rotating cylinders, and their correlations with the Reynolds number, rotation speed, and Mach number.

## II.   Spectral Difference Method

Until recently, compressible flow computations on unstructured meshes have generally been dominated by schemes restricted to second order accuracy. However, the need for highly accurate methods in applications such as vortex dominated flow, large eddy simulation, direct numerical simulation, computational aero-acoustics etc., has seen the development of higher order schemes for unstructured meshes such as the Discontinuous Galerkin (DG) Method,[26] Spectral Volume (SV) method[23] and Spectral Difference (SD) Method.[19–21] The SD method is a newly developed efficient high-order approach based on differential form of the governing equation. It was originally proposed by Liu et al.[20] and developed for wave equations in their paper on triangular grids.Wang et al.[21] extended it to 2D Euler equations on triangular grids and Liang[19] improved the convergence of the method using implicit LU-SGS and p-multigrid schemes.

Recently, Sun et al.[22] further developed it for three-dimensional Navier-Stokes equations on hexahedral unstructured meshes. The SD method combines elements from finite-volume and finite-difference techniques. Similar to the discontinuous Galerkin (DG) and spectral volume (SV) methods, the SD scheme achieves high-order accuracy by locally approximating the solutions as a high degree polynomial inside each cell. However, being based on the differential form of the equations, its formulation is simpler than that of the DG and SV methods since no test function or surface integral is involved. Conservation properties are still maintained by a judicious placement of the nodes at quadrature points of the chosen element.

## III.   Numerical Formulation

Consider the unsteady compressible 2D Navier Stokes equations in conservative form

American Institute of Aeronautics and Astronautics

$$\frac{\partial Q}{\partial t} + \frac{\partial F}{\partial x} + \frac{\partial G}{\partial y} = 0 \tag{1}$$

where $Q$ is the vector of conserved variables; $F$ and $G$ are the total fluxes including both inviscid and viscous flux vectors. To achieve an efficient implementation, all elements in the physical domain $(x, y)$ are transformed into a standard square element ($0 \leq \xi \leq 1$, $0 \leq \eta \leq 1$). The transformation can be written as:

$$\left( \begin{array}{c} x \\ y \end{array} \right) = \sum_{i=1}^{K} M_i(\xi, \eta) \left( \begin{array}{c} x_i \\ y_i \end{array} \right) \tag{2}$$

where $K$ is the total number of points used to define the physical element, $(x_i, y_i)$ are the cartesian coordinates of those points, and $M_i(\xi, \eta)$ are the shape functions. For elements with straight edges, K is equal to 4. For elements lying on curved boundaries, 8 points (four mid-edge and four corner points) can define a quadratic representation and 12 points can determine a third-order cubic representation. The metrics and the Jacobian of the transformation can be computed for each element. The governing equations in the physical domain are then transferred into the computational domain, and the transformed equations take the following form:

$$\frac{\partial \tilde{Q}}{\partial t} + \frac{\partial \tilde{F}}{\partial \xi} + \frac{\partial \tilde{G}}{\partial \eta} = 0 \tag{3}$$

where $\tilde{Q} = |J| \cdot Q$ and

$$\left( \begin{array}{c} \tilde{F} \\ \tilde{G} \end{array} \right) = |J| J^{-1} \left( \begin{array}{c} F \\ G \end{array} \right) \tag{4}$$

In the standard element, two sets of points are defined, namely the solution points and the flux points.

In order to construct a degree $(N-1)$ polynomial in each coordinate direction, solutions at $N$ points are required. The solution points in 1D are chosen to be the Gauss points defined by:

$$X_s = \frac{1}{2} \left[ 1 - cos\left( \frac{2s-1}{2N} \cdot \pi \right) \right], s = 1, 2, \cdots, N. \tag{5}$$

The flux points are selected by Sun et al[22] to be the Gauss-Lobatto points given by

$$X_{s+1/2} = \frac{1}{2} \left[ 1 - cos\left( \frac{s}{N} \cdot \pi \right) \right], s = 0, 1, \cdots, N. \tag{6}$$

Different flux points, however, are chosen for the computations in this paper. As suggested by Huynh[33] the flux points were selected to be Legendre-Gauss quadrature points plus the two end points 0 and 1. Choosing $P_{-1}(\xi) = 0$ and $P_0(\xi) = 1$, the higher-degree Legendre polynomials can be determined as:

$$P_n(\xi) = \frac{2n-1}{n}(2\xi - 1)P_{n-1}(\xi) - \frac{n-1}{n}P_{n-2}(\xi) \tag{7}$$

The locations of these Legendre-Gauss quadrature points are the roots of equation $P_n(\xi) = 0$. They are generally found to be more stable than the Gauss-Lobatto flux points.

Using the solutions at $N$ solution points, a degree $(N-1)$ polynomial can be built using the following Lagrange basis:

$$h_i(X) = \prod_{s=0, s\neq i}^{N} \left( \frac{X - X_s}{X_i - X_s} \right) \tag{8}$$

Similarly, using the fluxes at $(N+1)$ flux points, a degree $N$ polynomial can be built for the flux using a similar Lagrange basis:

$$l_{i+1/2}(X) = \prod_{s=0, s\neq i}^{N} \left( \frac{X - X_{s+1/2}}{X_{i+1/2} - X_{s+1/2}} \right) \tag{9}$$

The reconstructed solution for the conserved variables in the standard element is just the tensor products of the two one-dimensional polynomials,

$$\tilde{Q}(\xi, \eta) = \sum_{j=1}^{N} \sum_{i=1}^{N} \tilde{Q}_{i,j} h_i(\xi) \cdot h_j(\eta) \tag{10}$$

American Institute of Aeronautics and Astronautics

Similarly, the reconstructed flux polynomials take the following form:

$$\tilde{F}(\xi, \eta) = \sum_{j=1}^{N} \sum_{i=0}^{N} \tilde{F}_{i+1/2,j} l_{i+1/2}(\xi) \cdot h_j(\eta),$$

$$\tilde{G}(\xi, \eta) = \sum_{j=0}^{N} \sum_{i=1}^{N} \tilde{G}_{i,j+1/2} h_i(\xi) \cdot l_{j+1/2}(\eta) \tag{11}$$

The reconstructed fluxes are only element-wise continuous, but discontinuous across cell interfaces. For the inviscid flux, a Riemann solver is employed to compute a common flux at interfaces to ensure conservation and stability. In our case, we have used the Riemann problem solver (Rusanov[27] or Roe[28] with entropy fixing approach like[29]) to compute the interface fluxes.

In summary, the algorithm to compute the inviscid flux derivatives consists of the following steps:

- Given the conservative variables at the solution points, the conservative variables are computed at the flux points

- The inviscid fluxes at the interior flux points are computed using the solutions computed at the previous step

- The inviscid fluxes at the element interfaces are computed using the Rusanov/Roe solver. Given the normal direction of the interface n, and the averaged normal velocity component $V_n$ and the sound speed c, the inviscid flux on the interface can be determined.

- The derivatives of the fluxes are computed at the solution points using the derivatives of Lagrange operators $l$

$$\left(\frac{\partial \tilde{F}}{\partial \xi}\right)_{i,j} = \sum_{r=0}^{N} \tilde{F}_{r+1/2,j} \cdot l'_{r+1/2}(\xi_i),$$

$$\left(\frac{\partial \tilde{G}}{\partial \eta}\right)_{i,j} = \sum_{r=0}^{N} \tilde{G}_{i,r+1/2} \cdot l'_{r+1/2}(\eta_j) \tag{12}$$

We write inviscid and viscous fluxes separately for equation 1 as:

$$\frac{\partial Q}{\partial t} + \nabla F_e(Q) - \nabla F_v(Q, \nabla Q) = 0 \tag{13}$$

where the conservative variables Q and Cartesian components $f_e(Q)$ and $g_e(Q)$ of the inviscid flux vector $F_e(Q)$ are given by

$$Q = \left\{ \begin{array}{c} \rho \\ \rho u \\ \rho v \\ E \end{array} \right\}, \quad f_e(Q) = \left\{ \begin{array}{c} \rho u \\ \rho u^2 + p \\ \rho uv \\ u(E + p) \end{array} \right\}, \quad g_e(Q) = \left\{ \begin{array}{c} \rho v \\ \rho uv \\ \rho v^2 + p \\ v(E + p) \end{array} \right\} \tag{14}$$

Here $\rho$ is the density, $u$ and $v$ are the velocity components in x and y directions, p stands for pressure and E is the total energy. The pressure is related to the total energy by

$$E = \frac{p}{\gamma - 1} + \frac{1}{2}\rho(u^2 + v^2) \tag{15}$$

with a constant ratio of specific heat $\gamma$. For all test cases in the present study, $\gamma$ is going to be 1.4 for air.

The Cartesian components $f_v(Q, \nabla Q)$ and $g_v(Q, \nabla Q)$ of viscous flux vector $F_v(Q, \nabla Q)$ are given by

$$f_v(Q, \nabla Q) = \mu \begin{Bmatrix} 0 \\ 2u_x + \lambda(u_x + v_y) \\ v_x + u_y \\ u[2u_x + \lambda(u_x + v_y)] + v(v_x + u_y) + \frac{C_p}{P_r}T_x \end{Bmatrix},$$

$$g_v(Q, \nabla Q) = \mu \begin{Bmatrix} 0 \\ v_x + u_y \\ 2v_y + \lambda(u_x + v_y) \\ v[2v_y + \lambda(u_x + v_y)] + u(v_x + u_y) + \frac{C_p}{P_r}T_y \end{Bmatrix} \tag{16}$$

where $\mu$ is the dynamic viscosity, $C_p$ is the specific heat and $P_r$ stands for Prandtl number. T is temperature which can be derived from the perfect gas assumption. $\lambda$ is set to $-2/3$ according to the Stokes hypothesis.

The solution procedures to get viscous fluxes can be described as the following steps.

- reconstruct $Q_f$ at the flux points from the conservative variables at the solution points using equation 10.

- average the field of $Q_f$ on the element interfaces as $\overline{Q_f} = \frac{1}{2}(Q_f^L + Q_f^R)$. For interior flux points, $\overline{Q_f} = Q_f$. Meanwhile, appropriate boundary conditions shall be applied for specific edge flux points.

- evaluate $\nabla Q$ from $\overline{Q_f}$ using equation 12 where $\nabla Q = \begin{Bmatrix} Q_x \\ Q_y \end{Bmatrix}$ and $Q_x = \frac{\partial Q}{\partial \xi}\xi_x + \frac{\partial Q}{\partial \eta}\eta_x$, etc.

- reconstruct $\nabla Q$, from equation 10 and applying appropriate boundary conditions for specific flux points and average them on the element interfaces as $\overline{\nabla Q_f} = \frac{1}{2}(\nabla Q_f^L + \nabla Q_f^R)$

- use $\overline{Q_f}$ and $\overline{\nabla Q_f}$ in order to compute viscous flux vectors described in equation 16 at the element interfaces.

Flows with either steady or unsteady solutions are considered in this paper. In order to solve the flow to a steady state from a nearly arbitrary initial guess, a relaxation scheme is needed. Therefore, the time derivative term is retained for both steady and unsteady cases. All computations in this paper are advanced in time using a fourth-order strong-stability-preserving five-stage Runge-Kutta scheme.

# IV.   Numerical Validation

Two testing cases, a Taylor-Couette flow[32] (2009) and a laminar flow past a single cylinder[12] at Re=100, are presented here for validation of the flow solver.

## A.   Validation using compressible Taylor-Couette flow

In this example, the numerical order of accuracy is validated against the analytical solution for the compressible Taylor Couette flow. This test problem was taken from a recent paper presented by Michalak and Ollivier-Gooch.[30]

The Reynolds number based on the tangential velocity of the inner spinning cylinder and its radius (=1) is equal to 10. The temperature and pressure are prescribed for the inner cylinder giving a Mach number 0.5. The outer cylinder is fixed and an adiabatic wall boundary condition is employed. A grid with $24 \times 2$ cells is shown in figure 1. Two other finer grids are obtained using successive grid refinements in both directions. A steady solution of Mach number contour obtained by the SD method is shown in figure 1 (b). A cubic curved wall boundary is used for inner and outer cylinders. We obtained desired numerical order $L2$ accuracy of the y-direction velocity as shown in table 1. The maximum accuracy of fourth-order is demonstrated in the table. The explicit Runge-Kutta scheme becomes slow when the polynomial order is increased. However, the fifth-order and even higher accuracy can also be demonstrated using the implicit LU-SGS method and p-multigrid approach with a significantly shorter CPU time.[31]
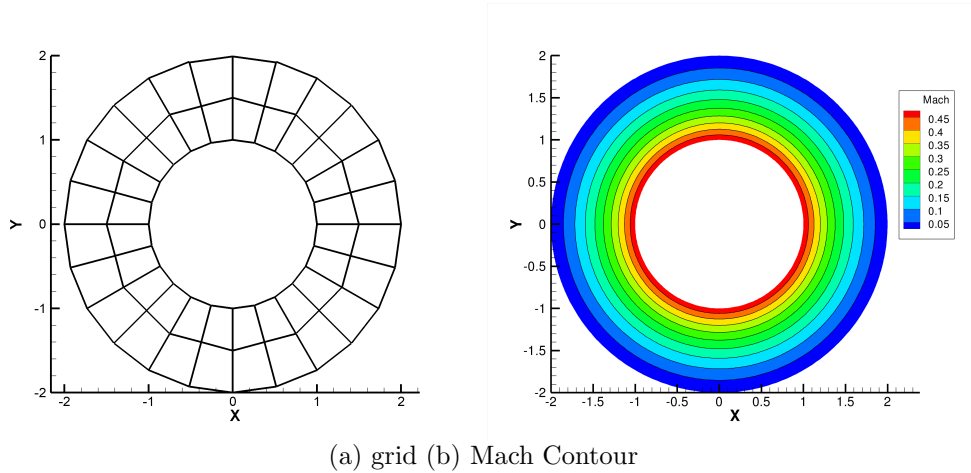
(a) grid (b) Mach Contour

**Figure 1.  Compressible Taylor Couette Flow**

| No. of elements | No. of DOFs | L2-error | Order |
|---|---|---|---|
| 3rd order SD | | | |
| 48 | 432 | 8.896E-04 | - |
| 192 | 1728 | 1.002E-04 | 3.15 |
| 768 | 6912 | 1.084E-05 | 3.21 |
| 4th order SD | | | |
| 48 | 768 | 1.4815E-04 | - |
| 192 | 3072 | 1.0036E-05 | 3.88 |
| 768 | 12288 | 6.5746E-07 | 3.93 |

**Table 1.  $L^2$ errors and orders of accuracy of viscous Taylor-Couette flow**

## B.    Validation using flow past a cylinder

Figure 2. shows the computational grid for the unsteady flow past a single cylinder.  There are 32 cells around the circumference of the cylinder.  The first cell near the cylinder wall has a spacing around 11% cylinder radius in the normal direction.  The level of grid resolution is much coarser than the one used in Meneghini et al.[13] who employed 128 points around the cylinder wall and the first node had a distance about 1% of cylinder radius for an isolated cylinder case.  The computation for this case is performed using 5th order SD method and a cubic curved wall boundary condition is employed for the cylinder surface.  Dirichlet boundary condition is used for the inlet and fixed-pressure is adopted for the outlet boundary condition. Invisicd symmetry boundary conditions are applied on the two lateral sides.

A snapshot of pressure contour is shown on the left hand side and the instantaneous velocity streamlines are illustrated on the right hand side in Figure 3.  The vortex formed by the fluid at the bottom of the cylinder is associated with a region of low pressure.  At this time instant, the unsteady lift coefficient is at its minimum.  The difference of coefficient $C'_L$ predicted by 4th order ($DOFs = 21,376$) and 5th order SD methods ($DOFs = 33,400$) is in the same order of the difference of coefficient $C'_D$ predicted by them.  These differences are all less than 2%.  For the single cylinder case, we only present the results obtained by 5th order SD method.

Table 2. reports the comparison between the present computation of compressible viscous flow at Mach number 0.2 to other numerical and experimental studies for incompressible viscous flow at the same Reynolds number 100.

The Strouhal number predicted by present SD method on a mesh with $DOF = 33,400$ is identical to the one predicted by Sharman[18] and the measured value by Williamson.[15]  There is a separate compressible flow simulation which is not included in the table.  Mittal[14] also predicted 0.164 using a finite element
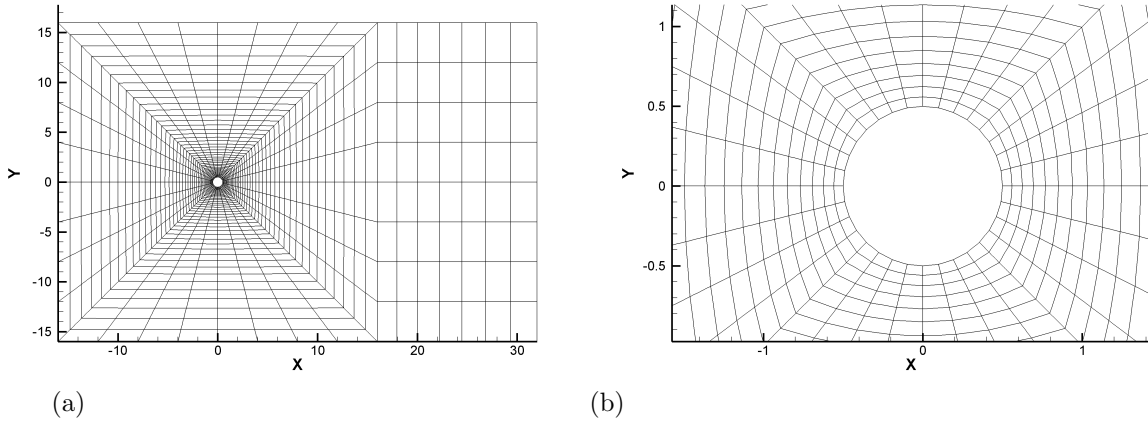
American Institute of Aeronautics and Astronautics

**Figure 2. Computational grid for unsteady flow past a cylinder**



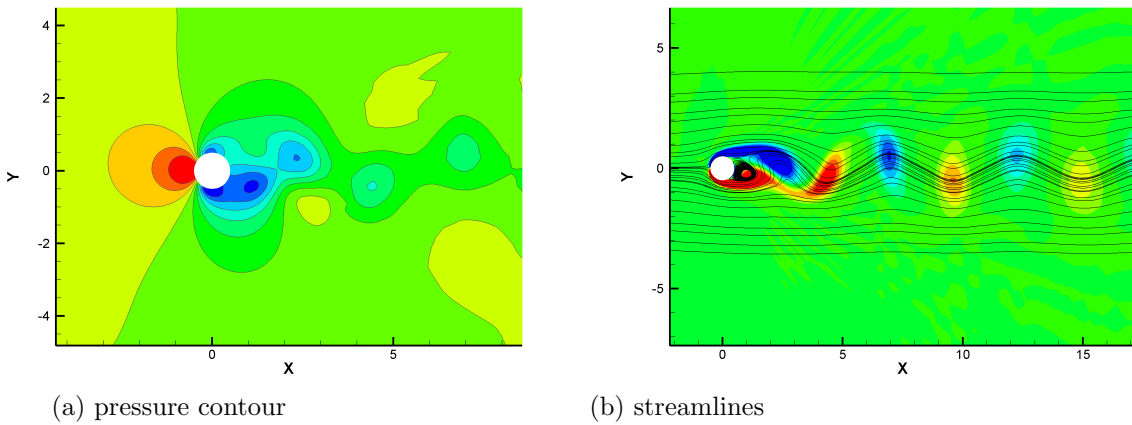(a) pressure contour                    (b) streamlines

**Figure 3. Instantaneous flow field computed for flow past a cylinder**

**Table 2. Computation Cases**

| Investigator | Present | Sharman 05 | Mene 01 | kang 03 | Ding 07 |
|---|---|---|---|---|---|
| Re no. | 100 | 100 | 100 | 100 | 100 |
| nodes | 1,336 | 14,441 | 13,696 | 62,127 | 23,033 |
| blockage | 0.0312 | 0.02 | 0.047 | - | - |
| $C_L'$ | 0.232 | 0.23 | - | 0.32 | 0.287 |
| $\overline{C_D}$ | 1.365 | 1.33 | 1.37 | 1.33 | 1.356 |
| $C_D'$ | 0.0086 | 0.0064 | - | - | 0.01 |
| St. no. | 0.164 | 0.164 | 0.165 | 0.165 | 0.166 |

compressible flow solver at $Re = 100$ and $Mach = 0.2$. The fluctuating lift coefficient is identical to the one predicted by the incompressible solver of.[16–18] The predicted higher $C_L'$ is probably due to insufficient near wall grid resolution and lower-order spatial piecewise schemes which are unable to resolve the wall curvature. The mean and rms drag coefficients are slightly higher than the ones predicted by Sharman.[18] However, the presently predicted $\overline{C_D}$ 1.365 is close to 1.37 predicted by Meneghini[13] and 1.356 predicted by Ding.[16] The low compressibility of the present flow condition may also slightly affect mean drag coefficient but its impact is certainly not noticeably strong. Mittal[14] also predicted the mean $C_D$ around the level of 1.4 as can be seen from figure 7 in their paper for Mach 0.2 and Re=100. Overall, this validation proves that our 2D spectral difference method produces the correct physics for flow past a cylinder.

# V.   Results and Discussion

In this section, we present numerical results for flow past two rotating cylinders in a side-by-side arrangement. We performed the simulations with the following conditions as listed in Table 3:

**Table 3. Computation Cases**

| Objectives | Fixed Paramters | Variable Parameter |
|---|---|---|
| Compressibility Effect | $g^* = 1, Re = 100, \omega = 3\Omega$ | $M = 0.05, 0.10, 0.20$ |
| Reynolds Number Effect | $g^* = 1, M = 0.10, \omega = 3\Omega$ | $Re = 1, 10, 20, 50, 100, 150$ |
| | $g^* = 1, M = 0.10, Re = 001$ | $\omega = 1\Omega, 2\Omega, 3\Omega, 4\Omega, 5\Omega$ |
| | $g^* = 1, M = 0.10, Re = 020$ | $\omega = 1\Omega, 2\Omega, 3\Omega, 4\Omega, 5\Omega$ |
| Rotation Speed Effect | $g^* = 1, M = 0.10, Re = 050$ | $\omega = 1\Omega, 2\Omega, 3\Omega, 4\Omega, 5\Omega$ |
| | $g^* = 1, M = 0.10, Re = 100$ | $\omega = 1\Omega, 2\Omega, 3\Omega, 4\Omega, 5\Omega$ |

Before presenting the above results, we first discuss the computational mesh and the boundary conditions pertaining to our two rotating cylinders flow geometry, and then carry out some further accuracy studies that are related to two rotating cylinders flow.

## A.   Computation Geometry and Conditions

The computation configuration is shown in Figure 4. In our computation, the geometry is non-dimensionalized so that the diameters of the cylinders are both equal to unity $D = 1$. The two cylinders are spaced at 2 units apart, measured from center to center, so that the gap to diameter ratio $g^* = 1$. The cylindrical rotation speed $\omega$ is measured in terms of $\Omega$, which is defined as $\Omega = 2U_\infty/D$.

American Institute of Aeronautics and Astronautics

The computational mesh has a cell number of $5,106$, with a total degree of freedom(DOFs) of $45,954$ for the 3rd order SD method, and 81,696 DOFs for the 4th order SD method. There are 60 cells along the periphery of the cylinder surface. The first cell near the cylinder wall is located at a distance of about 2.8% of the cylinder radius. A cubic curved boundary condition is applied for the wall. The present near wall grid resolution is finer than the one used by Kang[17](2003) with immersed boundary method.
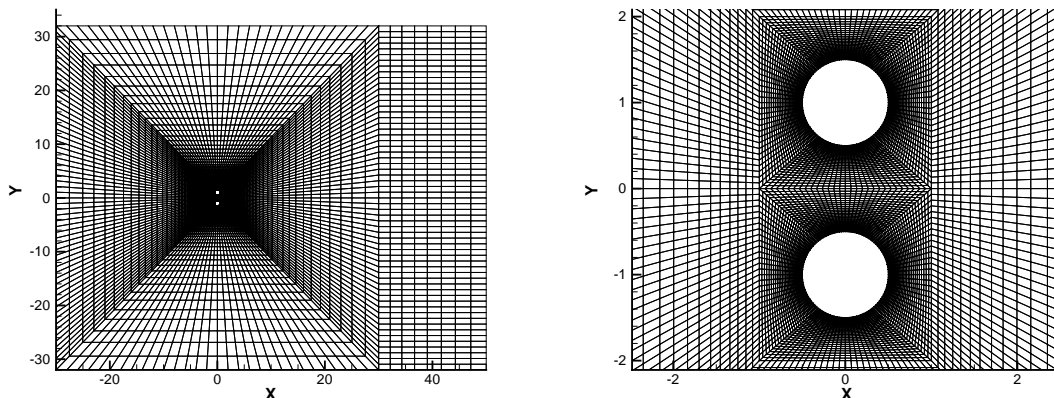


**Figure 4. Computation geometry and mesh. The left figure shows the entire flow field. The right figure shows the grid near the cylinders**

For the computational boundary conditions, we use iso-thermal wall boundary conditions. Dirichlet boundary condition is applied for the left inlet boundary. Symmetrical slip conditions are applied to the top and bottom boundaries. Fixed pressure is specified at the right boundary, and other values are extrapolated. The time step size used is: $h_{2nd} = 0.005$ for the second order SD method; $h_{3rd} = 0.001$ for the third order SD method; $h_{4th} = 0.0005$ for the fourth order SD method; and $h_{5th} = 0.0001$ for the fifth order SD method.

## B. Numerical Accuracy Study

The numerical accuracy and mesh independence study were carried out by implementing the 2nd, 3rd, 4th, and 5th order SD method at the same flow conditions of $Mach = 0.1$, $Re = 100$, $\omega = 3\Omega$, and $g^* = 1$. The results are tabulated in Table 4.

**Table 4. Numerical Accuracy and Grid Independence Study**

| SD Order | $CD_{pressure}$ | $CD_{shear}$ | $CD_{total}$ | $CL_{pressure}$ | $CL_{shear}$ | $CL_{total}$ |
|----------|-----------------|--------------|--------------|-----------------|--------------|--------------|
| 2nd | -0.3187 | 0.3405 | 2.18E-02 | 5.9843 | 0.3984 | 6.3827 |
| 3rd | -0.3122 | 0.3184 | 6.13E-03 | 5.8001 | 0.3793 | 6.1795 |
| 4th | -0.3154 | 0.3173 | 1.95E-03 | 5.7768 | 0.3783 | 6.1551 |
| 5th | -0.3153 | 0.3173 | 1.95E-03 | 5.7756 | 0.3783 | 6.1539 |

It is observed that, the 4th order approximation will be sufficient to lead to a mesh-independent result.

The simulations presented in the following section were performed with the 3rd order SD method unless otherwise noted.

## C. Result Comparison for Flow over Two Rotating Cylinders

Numerical study of flow past two rotating circular cylinders in a side-by-side arrangement has been carried out by several authors. In this section, we compare the numerical results of our SD simulations with those in the literature.

American Institute of Aeronautics and Astronautics

*1. Flow Condition: $Re = 100, g^* = 1.5, \omega = 1.2\Omega$*

Yoon et al.[9](2007) performed simulation, with immersed boundary method, at a range of low rotational speeds for four different gap spacings at Reynolds number of 100. This method used a two-step time-split scheme, and second-order accurate central difference scheme for the spatial discretization. The total number of mesh points used is 483 by 451. We performed the same simulation for the case with $g^* = 1.5$, $\omega = 1.2\Omega$, and $Re = 100$. The comparison is tabulated in Table 5.

**Table 5. Result Comparison with $g^* = 1.5$, $\omega = 1.2\Omega$, and $Re = 100$**

| Numerical Scheme | $CD_{total-max}$ | $CD_{total-min}$ | $CD_{total-ave}$ | $CL_{upper-ave}$ | $CL_{lower-ave}$ |
|---|---|---|---|---|---|
| 2nd Order SD | 0.82 | 0.68 | 0.75 | 3.1278 | -3.1279 |
| Yoon etl(2007) | 0.76 | 0.68 | 0.72 | 3 | -3 |

We compare the vorticity contour from Yoon (07) with our current SD method in Figure 5. The vorticity patterns look very similar.
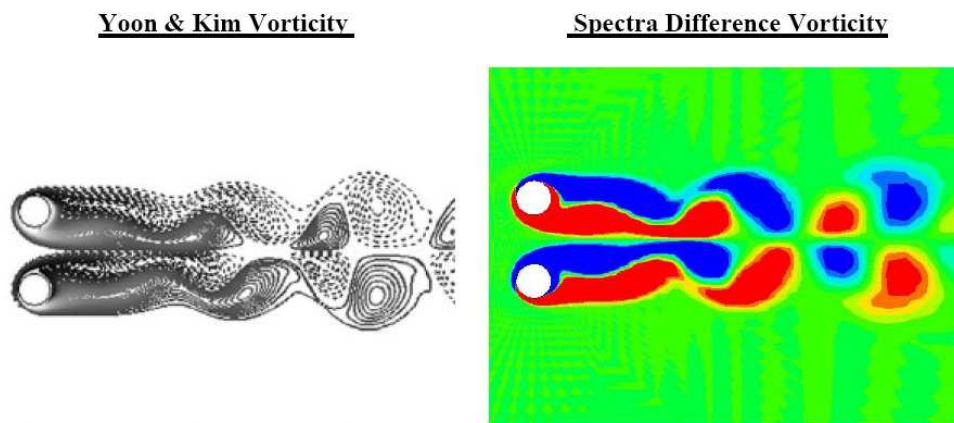


**Figure 5. Vorticity contours comparison between work by Yoon and the current SD method**

*2. Flow Condition: $Re = 150, g^* = 1, \omega = 1\Omega, 2\Omega, 3\Omega$*

Chan and Jameson[11] (2008) obtained numerical results of flow past two spinning cylinders using a commercial code CFD-ACE. The number of mesh cells used range between 150,000 and 200,000, with 280 grids along the cylinder surface. The simulations were performed at $Re = 150$, $g^* = 1$, and a wide range of rotation speeds. It was found that unsteady vortex wakes can be suppressed by increasing the rotation speed, and a virtual elliptic body formed by a closed streamline is observed. To make comparison, We performed the same simulations with the spectral difference method for the case with $g^* = 1$, $\omega = 1\Omega, 2\Omega, 3\Omega$, and $Re = 150$. The comparison is tabulated in Table 6.

We also performed the simulations under the same conditions with the industrial code StarCCM+. In Figure 6, we plot StarCCM+ results together with those of Chan and Jameson, and current SD method. The results match one another very closely.

For the remaining part of this section, we will present the numerical results for flow with various cylindrical rotation speeds, Reynolds numbers, and Mach numbers. We will start by investigating the change of flow characteristics at a fixed Reynolds number as the rotation speed increases, then studying the effects of changing the Reynolds numbers and freestream Mach numbers.

American Institute of Aeronautics and Astronautics

**Table 6.** **Results Comparison with work by Chan and Jameson (2008) for the case with** $g^* = 1$, $\Omega = 1, 2, 3$, **and** $Re = 150$

| Numerical Scheme | $CD_{total}$ | $CD_{pressure}$ | $CD_{shear}$ | $CL_{total}$ | $CL_{upper}$ | $CL_{lower}$ |
|---|---|---|---|---|---|---|
| $\Omega = 1$ | | | | | | |
| Spectral Difference | 0.809 | 0.271 | 0.538 | 0 | 2.528 | -2.528 |
| *Chan&Jameson* | 0.781 | 0.292 | 0.491 | 0 | 2.702 | -2.702 |
| $\Omega = 2$ | | | | | | |
| Spectral Difference | 0.169 | -0.115 | 0.284 | 0 | 5.025 | -5.025 |
| *Chan&Jameson* | 0.186 | -0.099 | 0.285 | 0 | 5 | -5 |
| $\Omega = 3$ | | | | | | |
| Spectral Difference | 0.012 | -0.239 | 0.251 | 0 | 5.8 | -5.8 |
| *Chan&Jameson* | 0.0188 | -0.258 | 0.277 | 0 | 6 | -6 |



(a) CL vs Rotation Re=150       (b) CD vs Rotation Re=150
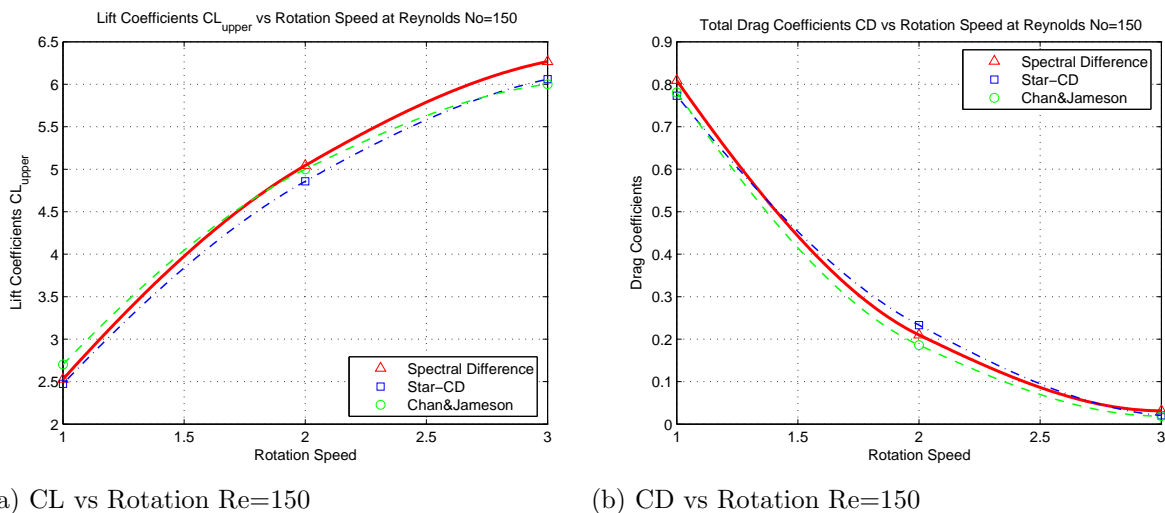
**Figure 6.** **Lift and Drag Coefficients Comparison for Flow Past Two Rotating Cylinders with** $Re = 150$, $g^* = 1$, **and** $\omega = 1\Omega, 2\Omega, 3\Omega$

## D. Effect of Rotation Speeds

For flow past two counter rotation cylinders in a side-by-side configurations in a viscous fluid, early work by Jeffery[1](1922) predicted that, as the rotation speed increases, a certain rotation rate will be reached whereby the force acting on the cylinders vanishes. Although Jeffery's theoretical work involves simplifications of the full flow physics, as his work was being refined by many other authors,[2–5] it was recognized that counter-spinning cylinders in this fashion can lead to significant drag reduction. This has been demonstrated numerically by various authors.[8, 9, 11]

Most of the existing literature, except Chan and Jameson (2008), have simulations performed at rotation speeds less than $2.5\Omega$. The lift and drag and the flow characteristics beyond that rotation rate are not well known. More significantly, Jeffery's approximate theoretical derivation points to a zero net-force solution at a rotation speed of $4\Omega$. To see this, the counter-rotating equal cylinders induced far field steady flow speed is given by $U_\infty = \frac{\omega r^2}{d}$, as derived by Jeffery, and since the gap spacing $g^* = 1$ leads to a center-to-center distance of $d = 2D$, the rotation speed that will induce a freestream velocity of $U_\infty$ is given by: $\omega = \frac{4 \cdot 2 U_\infty}{D} = 4\Omega$.

In this section, we present the lift and drag coefficients as a function of rotation speeds from $1\Omega$ to $5\Omega$. The cases of a low Reynolds number flow($Re = 1$), and moderate Reynolds number flow($Re = 50$) are discussed. We note here that the flow characteristics for Reynolds number 20, 50, 100, and 150 are very

American Institute of Aeronautics and Astronautics

similar. We select $Re = 50$ case to avoid unnecessary repetition. The effect of changing Reynolds number will be further discussed in the following section.

The lift coefficient, $C_L$, and the drag coefficient, $C_D$, consist of a pressure component and a shear component. We denote the pressure component by a subscript p, and the shear component by a subscript s such that $C_L = C_{Lp} + C_{Ls}$, and $C_D = C_{Dp} + C_{Ds}$.

Due to the symmetry of the flow under steady state condition, which can generally be achieved by rotating faster than about $1.5\Omega$, the drag coefficients for the upper cylinder, the lower cylinder, and the combined cylinders pair are the same. Hence, unless otherwise stated, the term CD in the rest of the section refers to all of the above.

Again, under the steady flow at fast enough rotation rate, the lift coefficients for the upper and lower cylinders are mirror image of each other. Therefore, the total lift coefficient of the combined cylinders pair is zero. Hence, unless otherwise stated, the term CL in the rest of the section refers to the lift coefficient on the upper cylinder. The CL for the lower cylinder will have the same value with an opposite sign.

*1. Effect of Rotation at Low Reynolds number*

The variations of $C_L$, $C_{Lp}$, $C_{Ls}$, $C_D$, $C_{Dp}$, and $C_{Ds}$ with rotation speed $\omega$ are tabulated and plotted in Table 7 and Figure 7.

**Table 7. Variation of force coefficients as a function of rotation speeds, with $g^* = 1$, $Mach = 0.1$, and $Re = 1$**

| Rotation | $CD_{total}$ | $CD_{pressure}$ | $CD_{shear}$ | $CL_{total}$ | $CL_{upper}$ | $CL_{lower}$ |
|---|---|---|---|---|---|---|
| $1\Omega$ | 6.6432 | 3.3552 | 3.2881 | 3.2406 | 1.8872 | 1.3534 |
| $2\Omega$ | 4.5685 | 2.2479 | 2.3206 | 3.6030 | 2.1824 | 1.4206 |
| $3\Omega$ | 2.5149 | 1.1378 | 1.3772 | 3.6638 | 2.2637 | 1.4002 |
| $4\Omega$ | 0.4192 | -0.0119 | 0.4311 | 3.4592 | 2.1717 | 1.2876 |
| $5\Omega$ | -1.8938 | -1.3060 | -0.5878 | 2.9762 | 1.9270 | 1.0492 |

At low Reynolds number, $C_D$, $C_{Dp}$, and $C_{Ds}$ decrease monotonically with the rotation speed $\omega$. The drag on the cylinders vanishes at a rotation rate of $4.2\Omega$. Further increasing the rotation speed, a thrust is produced on the cylinders. The system becomes self-propelling.

The streamline patterns at increasing rotation speeds are plotted in Figure 8. We find that the flow is not separated even at very low rotation speed. A virtual ellipse around the cylinders pair is formed by the enclosed streamline. We observe a pattern that is very similar to a doublet potential flow.

*2. Effect of Rotation at moderate Reynolds number*

**Table 8. Variation of force coefficients as a function of rotation speeds, with $g^* = 1$, $Mach = 0.1$, and $Re = 50$**

| Rotation | $CD_{total}$ | $CD_{pressure}$ | $CD_{shear}$ | $CL_{total}$ | $CL_{upper}$ | $CL_{lower}$ |
|---|---|---|---|---|---|---|
| $1\Omega$ | 1.0504 | 0.5633 | 0.4871 | 2.7852 | 2.4773 | 0.3078 |
| $2\Omega$ | 0.3817 | -0.1143 | 0.4961 | 5.2852 | 4.7749 | 0.5103 |
| $3\Omega$ | -0.0522 | -0.5668 | 0.5146 | 7.3001 | 6.6562 | 0.6439 |
| $4\Omega$ | -0.1880 | -0.1175 | 0.987 | 1.3944 | 1.2958 | 0.0986 |
| $5\Omega$ | -0.543 | 0.2325 | -0.2868 | -5.7816 | -5.3176 | -0.4640 |

Flow at higher Reynolds numbers has different characteristics. As shown in Figure 10, increasing the rotation rate leads to a drag reduction as before. However, the drag no longer decreases linearly with increasing rotation speed. Instead, it becomes very small when the rotation speed is around $3\Omega$, and stays close to zero as the rotation increases further.

American Institute of Aeronautics and Astronautics
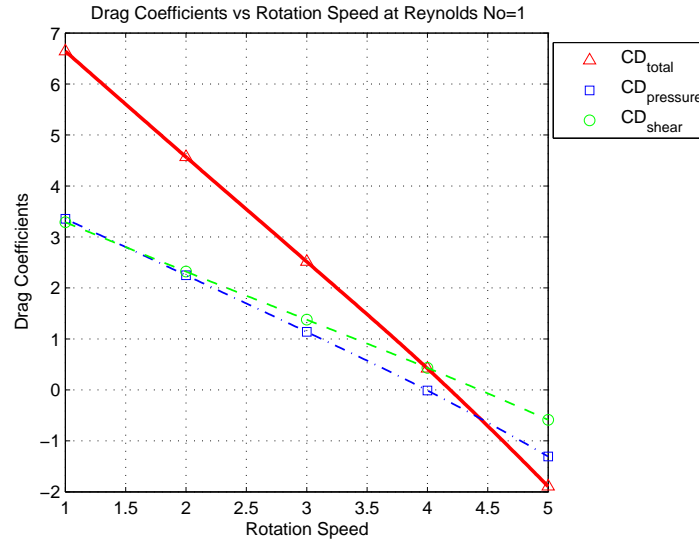
(a) CD vs Rotation Speeds at Re=1
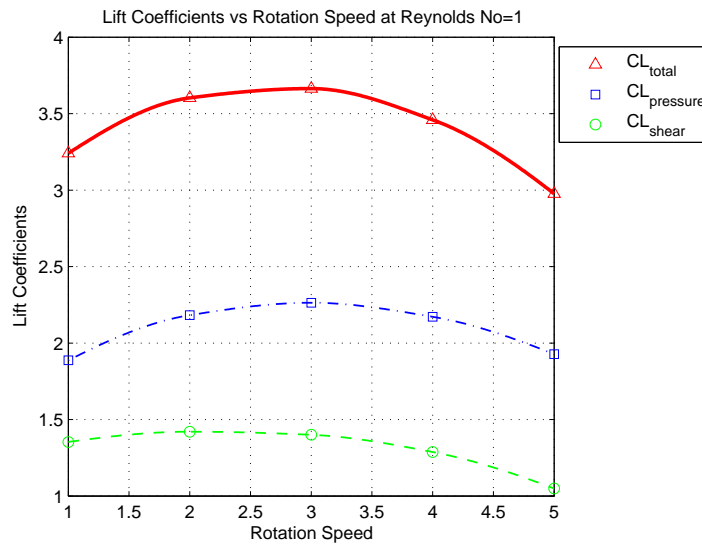


(b) CL (upper cylinder) vs Rotation Re=1

**Figure 7. Lift and Drag Coefficients with Increasing Rotation Speeds with $Re = 1$, $g^* = 1$, and $M = 0.1$**

We can divide the analysis into two parts. For rotation rate less than $3\Omega$, the pressure drag $C_{Dp}$ decreases rapidly while the shear drag $C_{Ds}$ stays more or less constant. Hence rotating the cylinders has a much more significant effect on the pressure drag, $C_{Dp}$, than on the shear drag, $C_{Ds}$. At moderate Reynolds numbers, the flow will usually separate behind non-rotating cylinders and form vortex wake. By increasing the rotation speed, we observe that the wake can be completely suppressed. The required rotation rate is near $2\Omega$. The decrease in pressure drag $C_{Dp}$ in this region is mainly due to this wake suppression effect. This can be readily perceived from the streamline patterns in Figure 11.

From $2\Omega$ to $3\Omega$, the streamline pattern changes drastically. The flow transits from a flow past two disjoint cylinders to a flow past a doublet-like body of cylinders pair. This changes the effective geometry of the system, and helps to reduce the drag of the system. We also observe that $C_{Dp}$ turns negative from around $2\Omega$, and its magnitude increases until it is about the same order of magnitude as $C_{Ds}$ at around $3\Omega$.

As the cylinders rotate faster beyond $3\Omega$, and the ellipse becomes more developed, the pressure contour shows this change clearly. A continuous pressure distribution in the shape of figure-of-8 is developed between the gap and the cylinders. The shear stress coefficient begins to decrease, as in the low Reynolds number

American Institute of Aeronautics and Astronautics
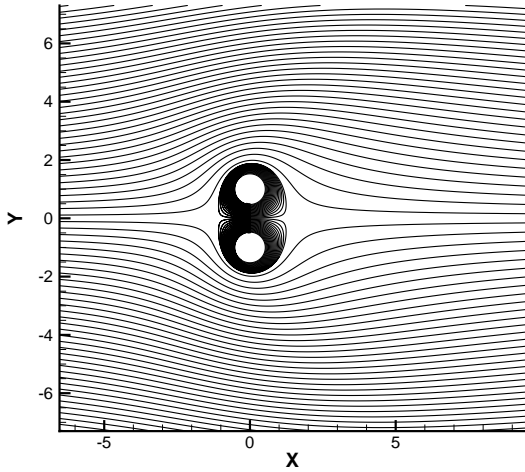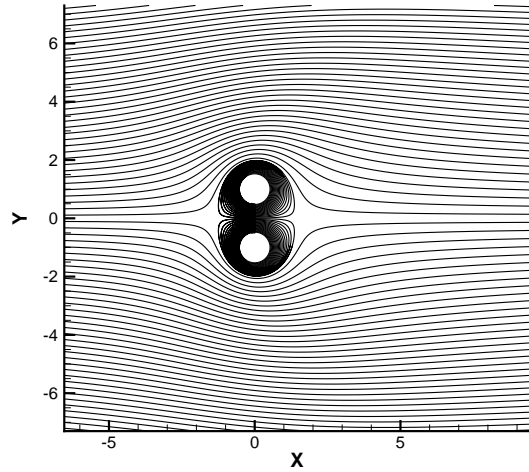
(a) Streamline at Re=1,$\omega = 1\Omega$      (b)Streamline at Re=1,$\omega = 2\Omega$
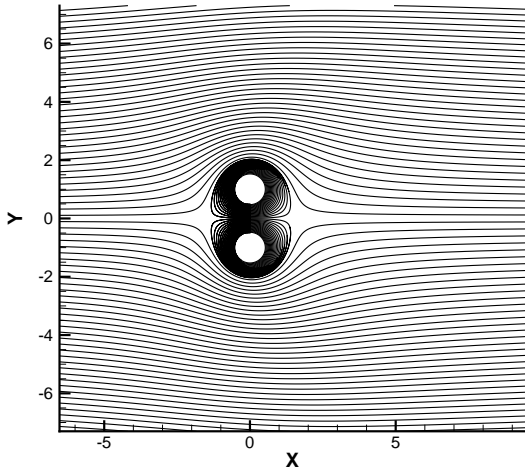
(c) Streamline at Re=1,$\omega = 3\Omega$      (d)Streamline at Re=1,$\omega = 4\Omega$
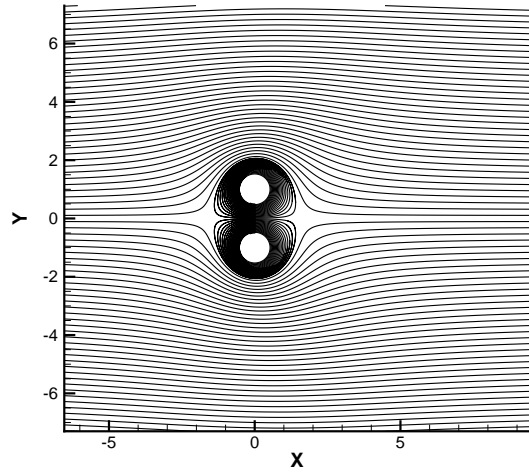
**Figure 8. Streamline Patterns with** $Re = 1$**,** $g^* = 1$**,**$M = 0.1$ **and** $\omega = 1\Omega, 2\Omega, 3\Omega, 4\Omega$

case, while the pressure drag coefficient begins to increase in roughly the same proportion. A self-equilibrium point is reached at around 4.2$\Omega$ whereby both the shear stress and pressure drag components nearly vanish.

However, unlike the low Reynolds number flow, the system of cylinders pair is no longer self-propelling beyond this critical rotation speed. Instead, the drag remains close to zero. We observe that, while the shear stress coefficient $C_{Ds}$ decreases monotonically in both low and moderate Reynolds number flow, the behavior of the pressure drag coefficient $C_{Dp}$ is very different. The increase in pressure drag component closely matches the increase in negative shear drag component, effectively producing very small net force on the cylinders.

### 3. Critical Rotation Rate for Minimum Force on Individual Cylinder

The simulation results show the existence of a critical rotation rate for minimum absolute force acting on each individual cylinder and the combined cylinders pair.

For the low Reynolds number flow, the pressure and shear drag coefficients vanish at a rotation speed of about 4.2$\Omega$. For the moderate Reynolds number flow, the $C_D$ becomes zero near 2.5$\Omega$ when the virtual

American Institute of Aeronautics and Astronautics
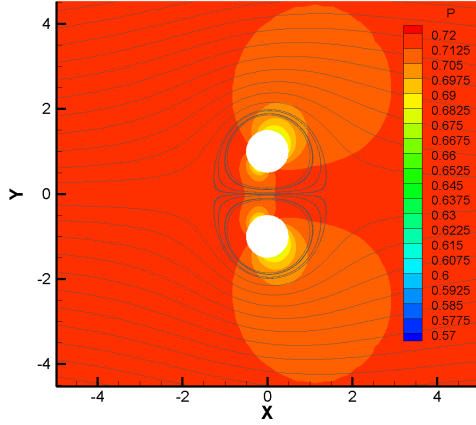
(a)Pressure Contour,Re=1,$\omega = 2\Omega$
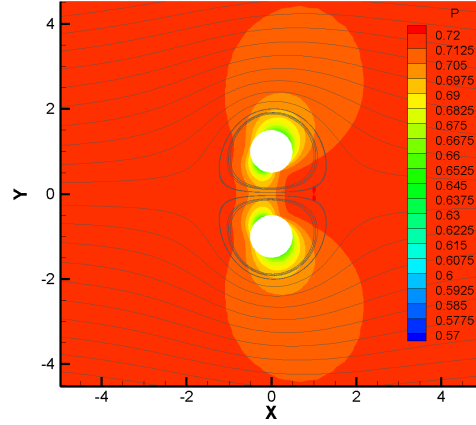
(b)Pressure Contour,Re=1,$\omega = 3\Omega$
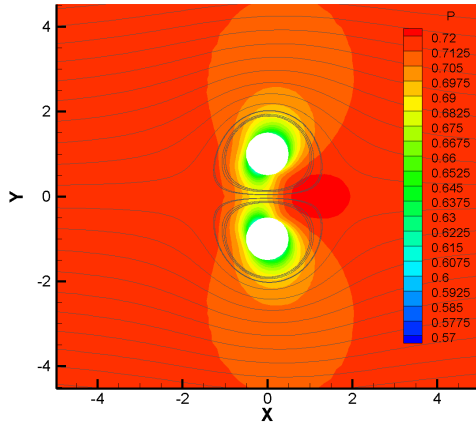
(c)Pressure Contour, Re=1,$\omega = 4\Omega$
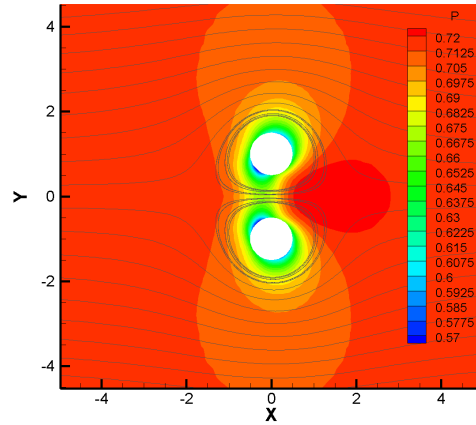
(d)Pressure Contour, Re=1,$\omega = 5\Omega$

**Figure 9. Pressure Contour for Flow Past Two Rotating Cylinders with** $Re = 1$, $g^* = 1$, $M = 0.1$ **and** $\omega = 2\Omega, 3\Omega, 4\Omega, 5\Omega$

elliptical body is beginning to form, but all six components ($C_L$, $C_{Lp}$, $C_{Ls}$, $C_D$, $C_{Dp}$, and $C_{Ds}$) vanish almost concurrently also around $4.2\Omega$.

To more clearly identify this critical rotation speed, the total absolute force coefficients at various rotation speeds and Reynolds numbers are plotted in Figure 13.

We observe that, regardless of Reynolds numbers, the rotation speed for minimum force acting on the individual cylinder invariably occurs at around $4\Omega$. Hence, by rotating at this speed, each individual cylinder is in the most equilibrium state with its surrounding fluid flow, and hence is subjected to minimum external stress. This is consistent with Jeffery's approximate theoretical result by matching the rotation speed $\omega$ with the self-induced freestream velocity $U_\infty$. For the non-dimensionalized cylinders gap $g^* = 1$, this rotation speed is, as shown previously, $\omega = 4\Omega$.

## E. Effect of Reynolds Number

In the previous section, we investigate the effect of rotation speeds on the flow characteristics at low and moderate Reynolds numbers. We notice that the flow behaves somewhat differently when the Reynolds number is different.

In particular, to summarize the key findings in the previous section, we observe that at low Reynolds
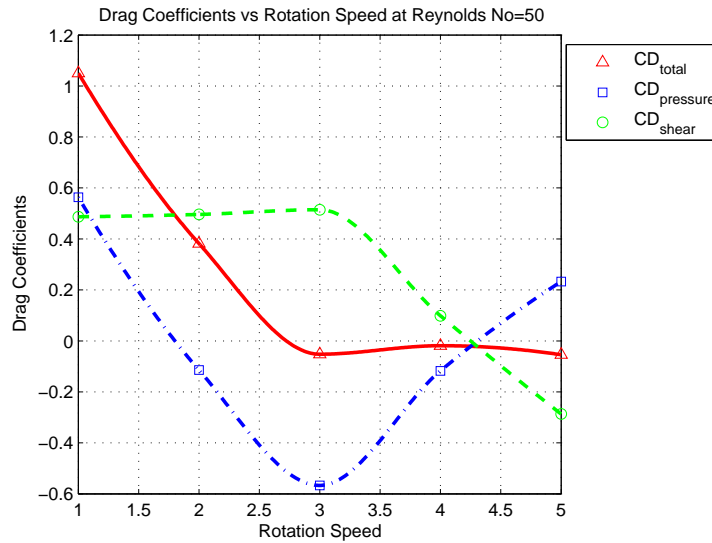
(a) CD vs Rotation Speeds at Re=50
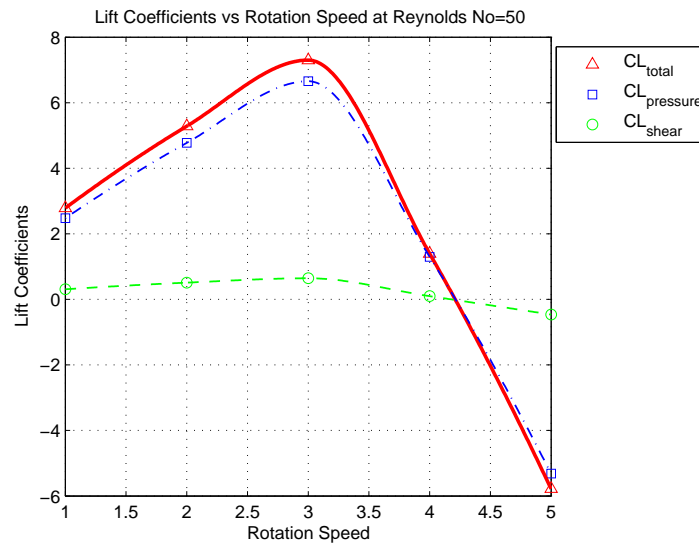


(b) CL (upper cylinder) vs Rotation Re=50

**Figure 10. Lift and Drag Coefficients with Increasing Rotation Speeds with $Re = 50$, $g^* = 1$, and $M = 0.1$**

number, firstly, the drag coefficients decreases almost linearly with increasing rotation speed; secondly, thrust is produced on the cylinders when the rotation speed is higher than the critical rotation rate; thirdly, the effect of rotation on the pressure and shear force components is very similar; and lastly the elliptical streamline pattern forms readily even at very low rotation speed. In contrast, at moderate Reynolds number, the drag decreases rapidly as the wake is being suppressed by cylinder rotation motion, then, once the elliptical streamline pattern enclosing the cylinders pair is formed, the streamwise force on the cylinders stays constant and remains very close to zero. The effect of rotation on pressure and shear drag is now equal and opposite so that, as they grow in magnitude but in the opposite direction, they effectively cancel each other out. In essence, the major difference between the low Reynolds number flow and the moderate Reynolds number flow can be largely attributed to the very different behavior of the pressure force component as the Reynolds number changes. The behavior of shear force component seems largely unaffected by Reynolds number.

In this section, we will quantify the difference by examining the flow at various rotation speeds at Reynolds numbers of 1, 20, 50, and 100. The force coefficients as a function of rotation speeds at various Reynolds numbers are plotted together in Figure 14.

American Institute of Aeronautics and Astronautics
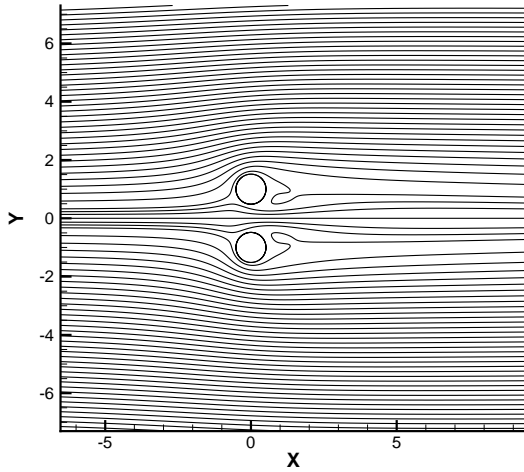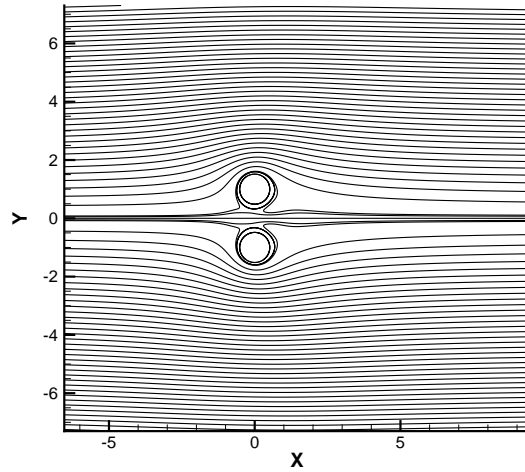
(a) Streamline at Re=50,$\omega = 1\Omega$        (b)Streamline at Re=50,$\omega = 2\Omega$
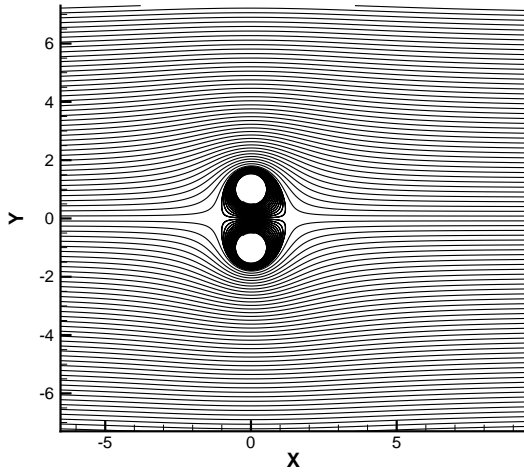
(c) Streamline at Re=50,$\omega = 3\Omega$        (d)Streamline at Re=50,$\omega = 4\Omega$
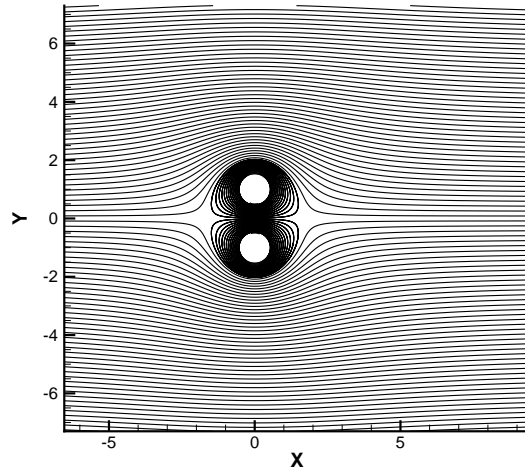
**Figure 11. Streamline Patterns with** $Re = 50$, $g^* = 1$,$M = 0.1$ **and** $\omega = 1\Omega, 2\Omega, 3\Omega, 4\Omega$

Except for very low Reynolds number, the flow for a wide range of moderate Reynolds numbers behave more or less the same as the rotation speed changes, and for rotation speed less than the critical rotation rate, the major effect of increasing Reynolds number on each individual cylinder here is to decrease the drag and increase the lift; on the combined cylinders pair, the net effect is a decrease in drag, as the net lift has always remained zero. This trend can be more clearly seen by plotting the force coefficients as a function of the Reynolds number at a fixed rotation speed of $3\Omega$ in Figure 15.

From these two sets of figures, we can make the following observations: firstly, for rotation speed less than the critical rotation rate, a critical Reynolds number exists whereby the drag on the cylinders reduces rapidly. This occurs in the $Re = 10 - 20$ region; secondly, the effect of the Reynolds number on drag is significant only for rotation speeds less than about $3\Omega$, beyond which the effect of Reynolds number is very small.
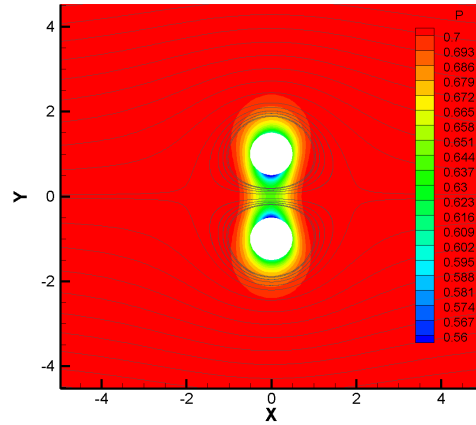
American Institute of Aeronautics and Astronautics
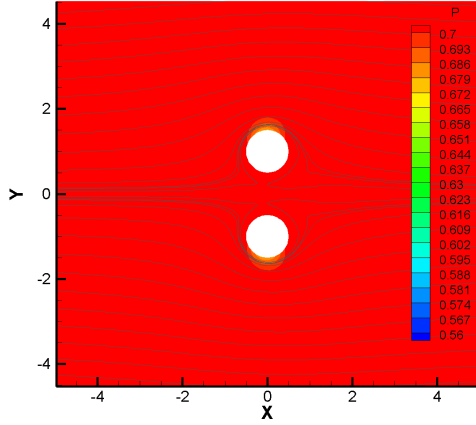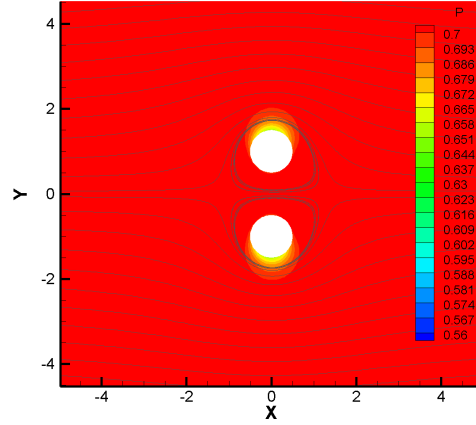
(a)Pressure Contour,Re=50,$\omega = 2\Omega$        (b)Pressure Contour,Re=50,$\omega = 3\Omega$
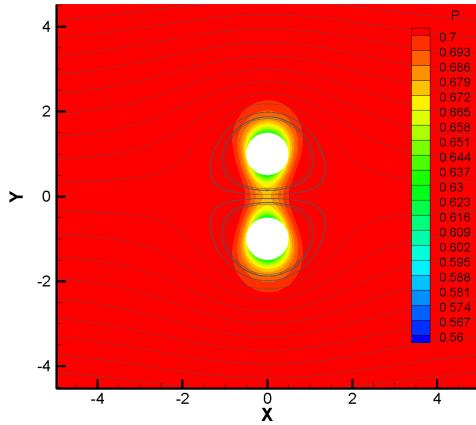
(c)Pressure Contour, Re=50,$\omega = 4\Omega$        (d)Pressure Contour, Re=50,$\omega = 5\Omega$

**Figure 12.  Pressure Contour with $Re = 50$, $g^* = 1$,$M = 0.1$ and $\omega = 2\Omega, 3\Omega, 4\Omega, 5\Omega$**

## F.    Effect of Compressibility

In this section, we investigate the effect of compressibility by performing the simulations at three different Mach numbers, $M = 0.05, 0.10, 0.20$, at a fixed Reynolds number and rotation speed of $Re = 100$, and $\omega = 3\Omega$.

**Table 9.  Variation of force coefficients as a function of Mach number, with $g^* = 1$, $\omega = 3\Omega$, and $Re = 100$**

| Mach Number | $CD_{total}$ | $CD_{pressure}$ | $CD_{shear}$ | $CL_{total}$ | $CL_{upper}$ | $CL_{lower}$ |
|---|---|---|---|---|---|---|
| 0.05 | 0.0363 | -0.2966 | 0.3330 | 6.2682 | 5.8872 | 0.3809 |
| 0.10 | 0.0217 | -0.3187 | 0.3404 | 6.3827 | 5.9843 | 0.3983 |
| 0.20 | -0.0036 | -0.4053 | 0.4017 | 7.3728 | 6.8637 | 0.5091 |

The variation of the force coefficients are plotted in Figure 16.  Increasing the Mach number increases the shear drag, decreases the pressure drag, and leads to a small decrease in the overall drag.  Increasing the Mach number increases the pressure lift,and the overall lift acting on each cylinder, but the net lift on the
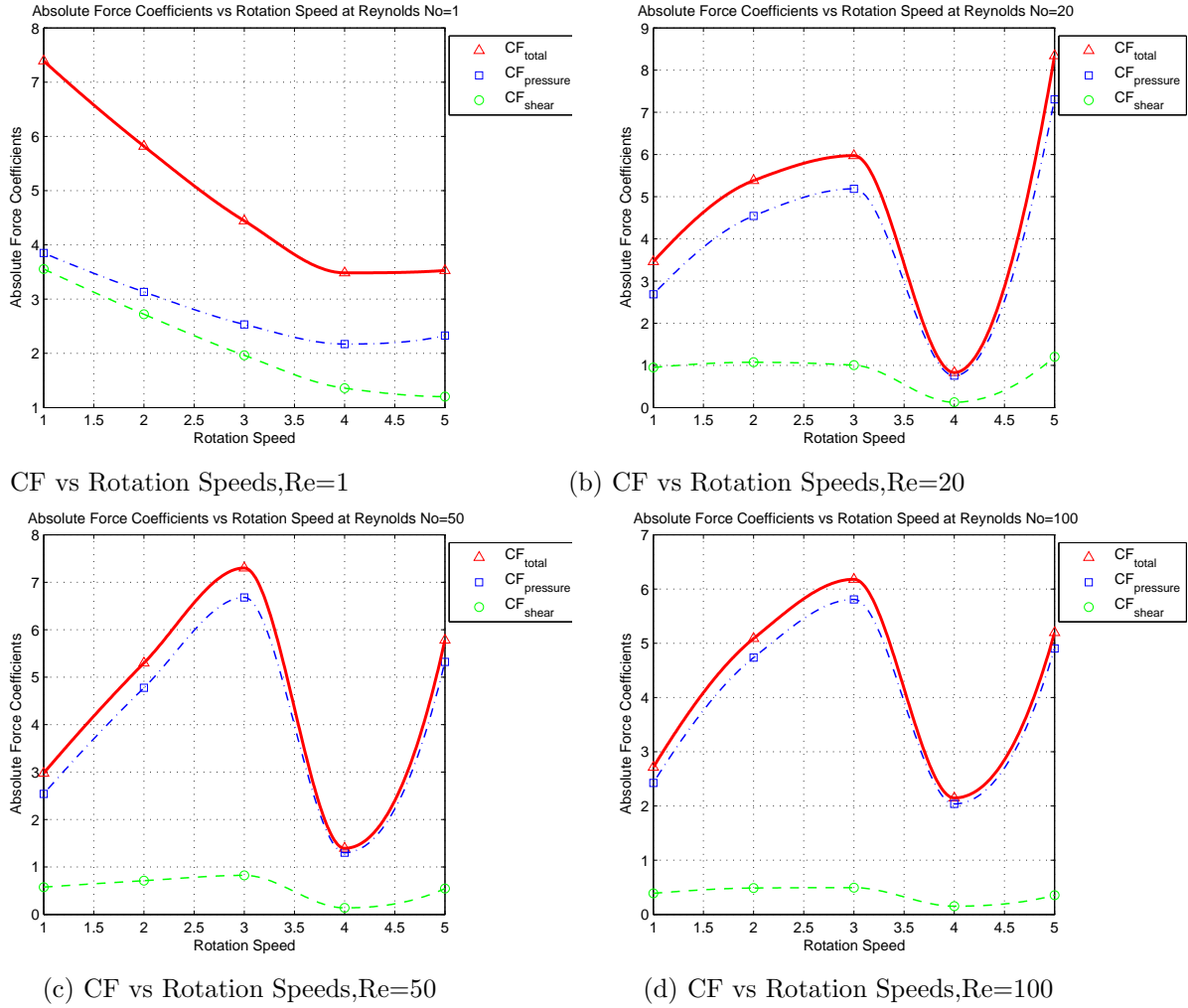
American Institute of Aeronautics and Astronautics

(a) CF vs Rotation Speeds,Re=1        (b) CF vs Rotation Speeds,Re=20





(c) CF vs Rotation Speeds,Re=50        (d) CF vs Rotation Speeds,Re=100

**Figure 13. Total Absolute Force Coefficients with Increasing Rotation Speeds with** $Re = 1, 20, 50, 100$**,** $g^* = 1$**, and** $M = 0.1$

cylinders pair, as always, remain zero.

The Mach and density contours are plotted in Figure 17. As the Mach number increases from 0.05 to 0.10 to 0.20, the density changes by 2%, 8%, and 30% respectively, and the maximum local Mach number increases from 0.16 to 0.3 to 0.65. We observe that, when the Mach numbers are low, the density and Mach contours look very similar. However, we do see a change in pattern as the Mach number increases. In particular, the figure-of-8 like pressure contour in between the cylinders is disappearing, implying that the elliptical streamline pattern is being weakened as the Mach number increases.

## VI. Conclusion

Flow past two counter rotating cylinders in a side-by-side arrangement has not been extensively studied numerically. The existing literature is limited both in terms of the physical scope of the numerical study as well as the numerical methods used to carry out those study. The goal of this paper is to implement a high-order accurate method to study such a flow over a wider range of Reynolds number, Mach number, and cylindrical rotation speed. To this end, we applied the 4th order spectral difference method in space, and five stage Runge-Kutta time stepping scheme, and cubic curved wall fitting to achieve high order of accuracy. Our obtained results compare favorably with existing data in the literature.

With our SD numerical scheme, we investigated the two rotating cylinders flow up to high rotation speeds. We find that counter rotating the cylinders results in the formation of an elliptical streamline
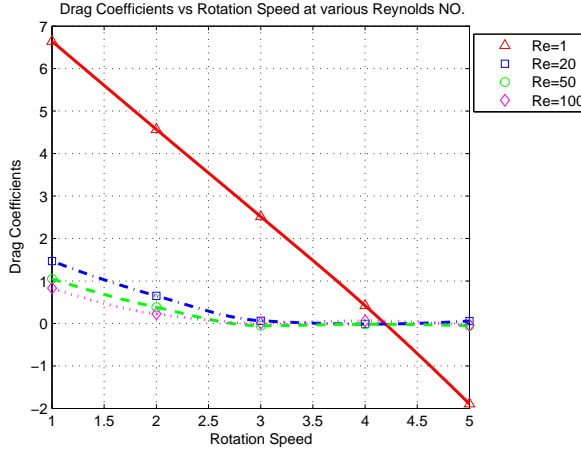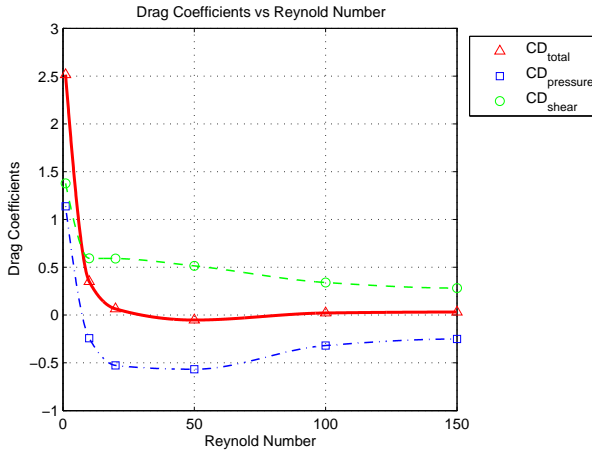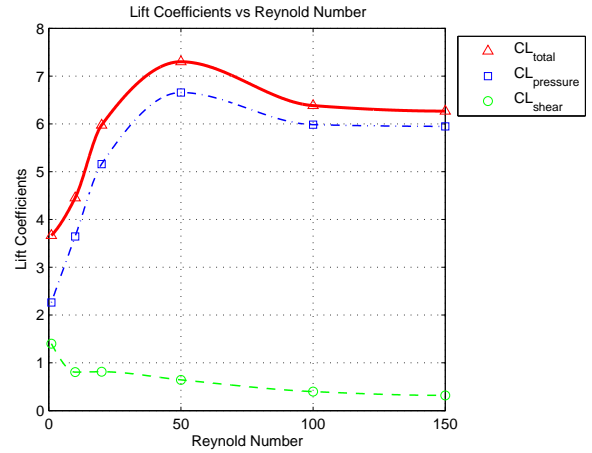
(a) CD vs Re at Various Rotation Speeds
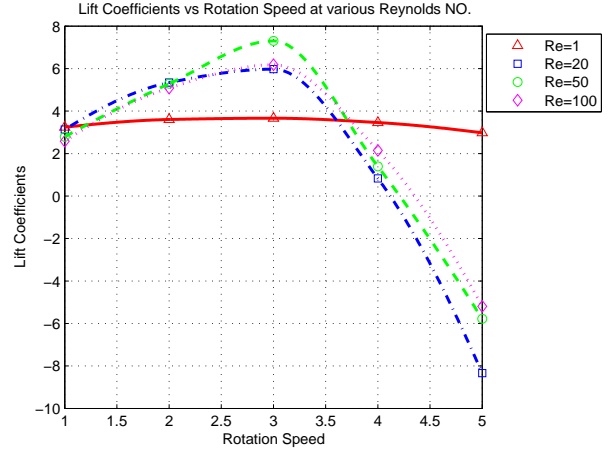


(b) CL vs Re at Various Rotation Speeds

**Figure 14. Lift and Drag Coefficients as a function of Reynolds number, with $Mach = 0.1$, $g^* = 1$, and $\omega = 1\Omega, 2\Omega, 3\Omega, 4\Omega, 5\Omega$**



(a) CD vs Reynolds number at $\omega = 3\Omega$



(b) CL vs Reynolds Number at $\omega = 3\Omega$

**Figure 15. Lift and Drag Coefficients as a function of Reynolds number, with $Mach = 0.1$, $g^* = 1$, and $\omega = 3\Omega$**

pattern enclosing the cylinders pair, which helps to suppress vortex wake and dramatically reduce the drag on the cylinders to a value very close to zero. For a wide range of moderate Reynolds number, the rotation speed required for the formation of elliptical streamline pattern is around $3\Omega$. Also, in the context of Jeffery's work on two counter-rotating cylinders in viscous flow, we identify a critical rotation rate of about $4.2\Omega$, at which the resultant force acting on each cylinder is minimum regardless of Reynolds number.

Our investigation of the Reynolds number effect shows that a Reynolds number of around $Re = 10 - 20$ exists which divide the flow physics into two rather different regimes. For lower Reynolds number, the cylinders pair is capable of self-propelling itself by rotating faster than the critical rotation rate of around $4.2\Omega$. For higher Reynolds number, fast rotation can at best achieve near zero drag. The flow in this regime is also not very sensitive to Reynolds number change.
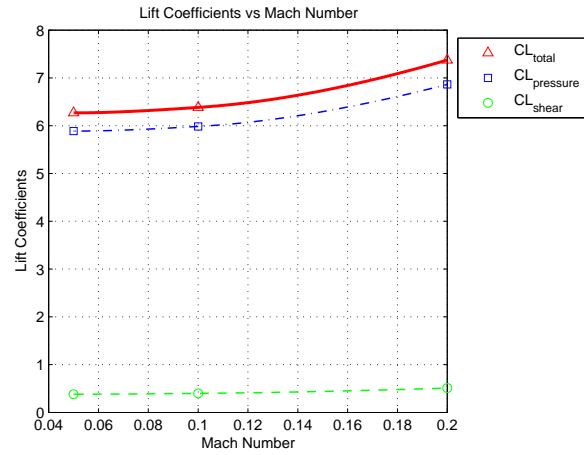
Lastly, we study the effect of compressibility and show that compressibility can have a slight drag benefit, and can also weaken the elliptical streamline pattern as the local Mach number becomes large.
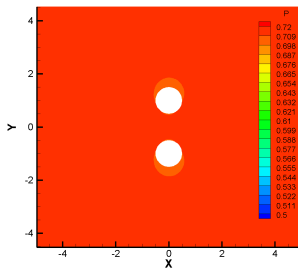
## VII.    Acknowledgement
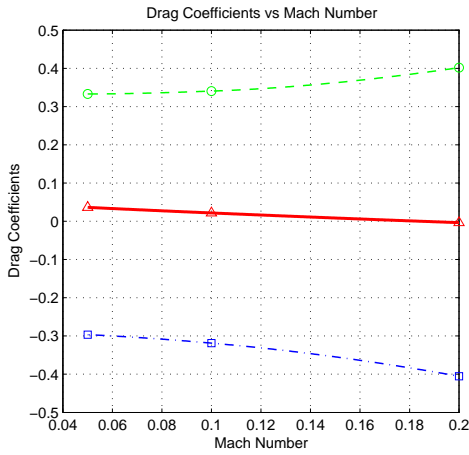
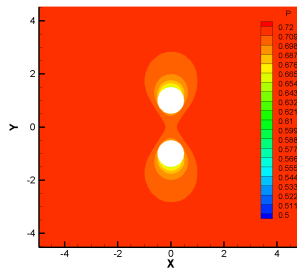(a) CD vs Mach at $Re = 100$, $\omega = 3\Omega$  (b) CL vs Mach at $Re = 100$, $\omega = 3\Omega$
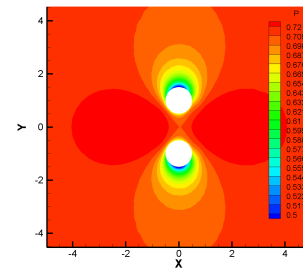
**Figure 16. Lift and Drag Coefficients as a function of Mach number, with $Re = 100$, $g^* = 1$, and $\omega = 3\Omega$**
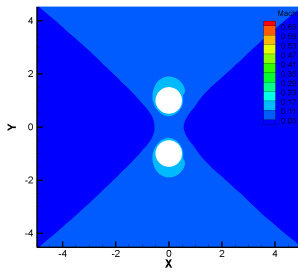


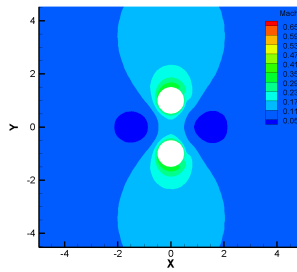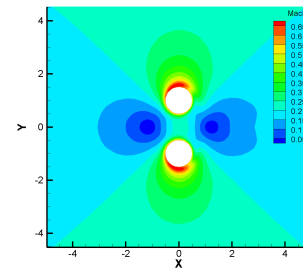(a)Pressure, M=0.05, $\omega = 3\Omega$  (b)Pressure, M=0.10, $\omega = 3\Omega$  (c)Pressure, M=0.20, $\omega = 3\Omega$



(a)Mach, M=0.05, $\omega = 3\Omega$  (b)Mach, M=0.10, $\omega = 3\Omega$  (c)Mach, M=0.20, $\omega = 3\Omega$

**Figure 17. Pressure (Top) and Mach (Bottom) Contour for Flow Past Two Rotating Cylinders with $Re = 100$, $g^* = 1$, $M = 0.05, 0.10, 0.20$ and $\omega = 3\Omega$**

# References

[1] G.B.Jeffery, The rotation of two circular cylinders in a viscous fluid, *Proceedings of the Royal Society*, 1922.

[2] E.J.Watson, Slow viscous flow past two rotating cylinders, *Mech.appl.Math)*,Vol 49, Pt. 2, 1996

[3] S.H.Smith, The rotation of two circular cylinders in a viscous fluid, *Mathematika*,Mathematika 38, 63-66, 1991

[4] Y.Ueda, A.Sellier, T.Kida & M.Nakanishi, On the low-Reynolds-number flow about two rotating circular cylinders,*J.Fluid Mech*, vol.495, pp. 255-281, 2003

[5] M.Nakanishi & T.Kida, Unsteady low Reynolds number flow past two rotating circular cylinders by a vortex method, *Proceedings of the 3rd ASME Conference*, 1999

[6] L.Elliott, D.B.Ingham & T.B.A.Ei Bashir, Stokes flow past two circular cylinders using a boundary element method, *Computers Fluids*,Computers Fluids 24, 787-798, 1995

[7]C.P.Hills, Flow patterns in a two-roll mill, *Q.JIMech.Appl.Math*, 2002

[8]S.Surattana & M.Nikolay, Numerical simulation of steady viscous flow past two rotating circular cylinders, *Suranaree J.Sci.Tech*, 2006

[9]H.S.Yoon,J.H.Kim, H.H.Chun & H.J.Choi, Laminar flow past two rotating cirucular cylinders in a side-by-side arrangement, *Physics of Fluids*, 2007

[10]A.J.Chorin, Numerical solution of the Navier-Stokes equations, *Math.Comp.*, 1968

[11]A.S.Chan & A.Jameson, Suppression of the unsteady vortex wakes of a circular cylinder pair by a doublet-like counter-rotation, *Stanford Report ACL 2008-1*, 2008

[12]C.H.Liang, S.Premasuthan & A.Jameson, High-order accurate simulation of low-Mach laminar flow past two side-by-side cylinders with spectral difference method,*Computers and Structures*,2008

[13]J. R. Meneghini, F. Saltara, C. L. R. Siqueira & J. A. Ferrari, Numerical simulation of flow interference between two circular cylinders in tandem and side-by-side arrangements,*J. Fluids and Structures*,2001

[14]S. Mittal & T. Tezduyar, A unified finite element formulation for compressible and incompressible flows using augmented conservation variables, *Computer Methods in Applied Mechanics and Engineering*,vol161,p229-243,1998

[15]C. H. K. Williamson, Oblique and parallel modes of vortex shedding in the wake of a circular cylinder at low Reynolds numbers,*Journal of Fluid Mechanics*,vol206, p579-627,1989,

[16]H. Ding, C. Shu, K. S. Yeo & D. Xu, Numerical simulation of flows around two circular cylinders by mesh-free least square-based finite difference methods,*Int. J. for Numer. Methods in Fluids*,vol53,p305-332,2007

[17]S. Kang,Characteristics of flow over two circular cylinders in a side-by-side arrangement at low Reynolds numbers,*Physics of Fluids*,vol15,p2486-2498,2003

[18]B. Sharman and F. S. Lien and L. Davidson and C. Norberg,Numerical predictions of low Reynolds number flows over two tandem circular cylinders,*Int. J. for Numerical Methods in Fluids*,vol47,p423-447,2005

[19]C. Liang, R. Kannan & ZJ Wang, A p-Multigrid Spectral Difference Method with explicit and implicit smoothers on unstructured grids, *AIAA paper*, AIAA-2007-4326, 2007.

[20]Y. Liu, M. Vinokur, & Z. J. Wang, Spectral difference method for unstructured grids I: Basic formulation, *J. of Comput. Phys.*, Vol. 216 , pp. 780-801, 2006.

[21]Z.J. Wang, Y. Liu, G. May and A. Jameson, Spectral Difference Method for Unstructured Grids II: Extension to the Euler Equations, *Journal of Scientific Computing*, Vol. 32, pp. 45-71, 2007.

[22]Y. Sun, Z. J. Wang, & Y. Liu, High-order multidomain spectral difference method for the Navier-Stokes equations on unstructured hexahedral grids, *Communication in Computational Physics*, Vol. 2, pp. 310-333, 2007.

[23]Y. Liu, M. Vinokur, & Z. J. Wang, Spectral (finite) volume method for conservation laws on unstructured grids V: Extension to three-dimensional systems, *Journal of Computational Physics*, Vol. 212, pp 454-472, 2006.

[24]Z. J. Wang & Y. Liu, Extension of the spectral volume method to high-order boundary representation, *Journal of Computational Physics*, Vol. 211, pp. 154-178, 2006.

[25]R. J. Spiteri, S. J. Ruuth, A new class of optimal high-order strong-stability-preserving time discretization methods, *SIAM J. Numer. Anal.*, Vol 40, pp 469-491, 2002

[26]F.Bassi and S. Rebay, High-order accurate discontinuous finite element solution of the 2D euler equations, *Journal of Computational Physics*, Vol. 138, pp. 251-285, 1997

[27]V. V. Rusanov, Calculation of interaction of non-steady shock waves with obstacles, *J. Comp. Math. Phys. USSR*, 1961

[28]P.L. Roe, Approximate Riemann Solvers, *Journal of Computational Physics*, 1981

[29]A Harten & J.M. Hyman, Self-adjusting grid methods for one-dimensional hyperbolic conservation laws, *Journal of Computational Physics*, 1983

[30]C. Michalak & C. Ollivier-Gooch, Unstructured High-Order Accurate Finite-Volume Solutions of the Navier-Stokes Equations, *AIAA paper*, AIAA-2009-954, 2009

[31]C. Liang, R. Kannan & ZJ Wang, A p-Multigrid Spectral Difference Method with explicit and implicit smoothers on unstructured triangular grids, *Computers and Fluids*, Vol. 38, pp. 254-265, 2009.

[32]A. Jameson, C. Liang, 'Unsteady flow past a plunging airfoil simulated with high-order Spectral Difference method', Workshop on Vortex Dominated Flows, June, 2009, National Institute of Aerospace

[33]H.T.Huynh, 'A flux Reconstruction Approach to High-Order Schemes Including Discontinous Galerkin Methods', AIAA paper, AIAA-2007-4079, 2007